Journal of Ultrafine Grained and Nanostructured Materials
https://jufgnsm.ut.ac.ir
Vol. 54, No.2, December 2021, pp. 149-162
Print ISSN: 2423-6845 Online ISSN: 2423-6837
DOI: 10.22059/jufgnsm.2021.02.04

Plasma electrolyte oxidation of hydroxyapatite-containing coating on AZ31B Mg alloy: Effects of current density and duty cycle

Razieh Chaharmahali, Arash Fattah-alhosseini*, Hamid Esfahani

Department of Materials Engineering, Bu-Ali Sina University, Hamedan, Iran.

Recieved: 25 June 2021; Accepted: 18 September 2021
**Corresponding author email: a.fattah@basu.ac.ir*

ABSTRACT

Plasma electrolytic oxidation (PEO) procedure has been considered as a proper method to increase the corrosion resistance of Mg alloys. In this study, the effect of current density and duty cycle as the operating parameters on the corrosion behavior of coatings at a constant frequency was studied. Also, hydroxyapatite nanoparticles were added to the electrolyte to improve the biological activity of the final coating. The top and cross-section view of the coatings was studied using scanning electron microscopy (SEM) to explore the microstructure changes by the operating parameters. The corrosion performance of coatings was evaluated by electrochemical impedance spectroscopy (EIS) and potentiodynamic polarization (PDP) assays in simulated body fluid (SBF), respectively. The appropriate current density selection of 300 mA/dm^2 and a duty cycle of 50 % confirmed the high corrosion resistance of obtained coating because of the morphology of the coating. At the optimum parameters, the results of the *in vitro* immersion test showed that the coating containing hydroxyapatite has higher biological activity, and also it could protect the coating for a longer period of time.

Keywords: *AZ31B Mg alloy; Plasma electrolytic oxidation (PEO); Operating parameters; Hydroxyapatite; Bioactive*

1. Introduction

Magnesium and its alloys are one of the most significant and widely used biodegradable materials that are utilized in diverse medical applications [1–6]. Generaly, magnesium is known as a proper biological material due to its good biocompatibility and biodegradability properties in addition to possessing favorable mechanical properties [7–9]. Indeed, magnesium is a non-toxic element that is naturally found in the body. The density and Young's modulus of Mg and its alloys are really similar to bone in comparison to other implants that declines the stress between the bone and the implant and rises bone growth and implant stability [10–12]. Nevertheless, the main problem of magnesium and its alloys is its high rate of corrosion in the body that restricts their usage. The amount of corrosion and its destruction in the body environment must be controlled to improve the usage of magnesium and its alloys as implants [13–16]. Different coating methods have been studied to protect magnesium and its alloys against corrosion including sol-gel methods, physical vapor deposition, and PEO [17–23]. PEO is one of the new kinds of surface modification technology to produce ceramic coatings on metals like aluminum [24–29], magnesium [30–38], zirconium [39–43], and titanium [44–49]as well as their alloys.

In comparison to general anodizing treatments, the PEO technique can consistently generate an oxide layer that strongly adheres to a substrate,

making it an excellent way to boost the corrosion resistance of Mg alloys or, as a pre-treatment, to improve the adherence for post coatings [50]. Coatings made from PEO have various advantages over other coatings. PEO-derived coatings are extremely hard and stable, and they can withstand high temperatures. Corrosion performance is better in PEO-derived coatings than in other chemical conversion layers [51,52]. Furthermore, the cracks and pores created in PEO-derived coatings during micro-arc discharges can assist reduce the coating's residual stress. The porous outer layer of PEO-derived coatings would result in increased binding strength at the adhesive–substrate interface of joints [53–55].

In this technique and by applying a variable potential between the anode and the cathode until it reaches the values of breakdown voltage, electrical discharges on the anode surface are used. Much heat is released here that results in electrochemical and thermochemical reactions in the plasma atmosphere that results in the production of a ceramic coating with a complex composition on the metal surface [56–60]. PEO-derived coatings have very desirable properties including high adhesion and hardness, favorable anti-corrosion properties, acceptable abrasion resistance, and high thermal stability [32,61–64]. Moreover, the microstructure of PEO-derived coatings reveals that due to the eruption of the reaction products from the discharge channels, they are inherently porous, and the surface contains several micro-cracks. After finishing the procedure, the surface has numerous cavities that results in a weakening of the properties of the coating to some extent. Porosity in PEO-derived coatings lets easy penetration of the electrolyte. The structure of the obtained PEO-derived coatings could be controlled by using a series of procedure parameters such as substrate, electrolyte, time, temperature, and additive as well as operating parameters like voltage, frequency, duty cycle, and current density. Among these, operating parameters are really dominant in the coating quality and properties. Among the operating parameters, researchers have inferred that current density and duty cycle influence the rate of growth and discharge characteristics of PEO-derived coatings [65–70]. Thus, the structure and thickness of the coatings are improved by adjusting the operating parameters. Tang et al. [71] examined various duty cycles. They saw that higher duty cycles augmented the porosity of film and gradually reduced the thickness of oxide film.

In this research, first the current density and then the duty cycle in coatings containing hydroxyapatite nanoparticles on magnesium alloy have been investigated that has caused to find major changes in the microstructure, morphology, and porosity of the coating that eventually improves the corrosion properties. In the end, the bioactivity behavior of the obtained coating with the most suitable microstructure and the highest corrosion behavior has been investigated in the body simulated fluid at distinct times.

2. Experimental Procedure

2.1. PEO process

A sheet of AZ31B having dimensions of 3 × 15 × 20 mm^3 was used to coat the rectangular samples. The surface and edge of the specimens were polished using sandpapers ranging from 220 to 2000. After sanding, the specimens were fully washed using distilled water and they were all dried by flowing cold air. A detailed description of the chemical composition of AZ31B Mg alloy can be found in previous publication [23]. Mg specimens are immersed in the electrolyte as an anode (positive pole) to carry out the coating procedure. A cooling system was utilized to control the temperature within the coating procedure. The used alkaline electrolyte contains KOH (3 g/l), Na_3PO_4 (5 g/l), and hydroxyapatite nanoparticles (15 g/l). All coatings are made at a frequency of 1000 Hz. The operating parameters in the coating procedure are shown in Table 1.

Table 1- Operating parameters, electrolyte composition and coating characteristic in the coating procedure

Code	Current density (mA/dm^2)	Frequency (Hz)	Duty cycle (%)	Electrolytic	pH	Conductivity	Thickness (μm)
300-50	300	1000	50	Na_3PO_4 (5 g/l) KOH (3 g/l) Hydroxyapatite nanoparticles (15 g/l)	13.40	18.02	36.1
350-50	350	1000	50				42.2
400-50	400	1000	50				45.3
300-20	300	1000	20				20.7
300-80	300	1000	80				44.2

2.2. Surface characterization of coating

The composition and surface morphology of PEO-derived coatings were studied using x-ray diffraction (XRD), energy dispersive X-ray spectrometer (EDS), and scanning electron microscopy (SEM). A detailed description of the XRD, EDS, and SEM instruments can be found in previous publication [23]. It should be noted that the calculation of porosity size and thickness of coatings was carried out using MIP software.

2.3. Corrosion measurements

The simulated body fluid (SBF) solution was prepared based on the Kokubo method [72] to carry out the potentiodynamic polarization (PDP) and electrochemical impedance spectroscopy (EIS) tests. A detailed description of the PDP and EIS tests can be found in previous publication [23].

2.4. Immersion test

Immersion tests in body simulated fluid were used to evaluate the bioactivity. Samples were prepared before being put in the simulated body fluid. An area of 1 cm^2 of each sample was considered so that not to be in contact with the body simulated fluid. In each container, a coated substrate was first put. About 10 ml of the simulated body fluid was added to each container. After closing the lid of the container, the container was put inside an incubator having an insulated chamber at a constant temperature of 37 ° C. All samples were removed from the solution after 1, 3, 5, and 7 days and then the coatings were washed using distilled water and dried at room temperature.

3. Results and Discussion

3.1. Voltage-time diagram

Fig. 1 reveals the voltage-time diagram for the coating procedure at distinct current densities and duty cycles in 7 minutes.

Based on the increase in the rate of voltage, the plot is generally divided into three steps. In the first step, the voltage of all specimens increases linearly with a high slope at different operating parameters. The electric field provides the driving force for the cations and anions transfer in the solution throughout the protective layer and helps to increase the thickness of the protective layer that shows the formation of an oxide film at the interface of the electrolyte and the metal. At this step, a lot of bubbles are released and no spark is produced. This step shows the procedure of the common anodizing procedure. As the thickness rises, the protective layer acts as a current resistor. After this, the dielectric breakdown of the protective film occurs in areas with lower resistance, resulting in the formation of small sparks at the breakdown voltage. At this stage, several white and light sparks will be present on the surface. In the third stage, the changes in voltage reach a stable value. The microdischarges alter to stronger sparks, and they stay prolonged time as their color shifts from white to orange. Voltage-time diagrams show that the ignition voltage increases as the applied current density increases. On the other hand, the passing time from the first and second stages decreases by rising current density, and reaching the third stage takes place faster [73–77].

On the other hand, the growth rate of high-resistance coatings rises and the thickness of

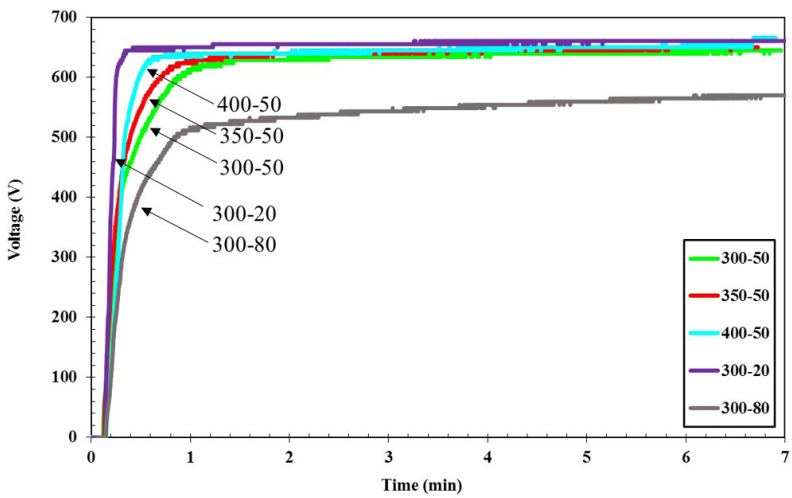

Fig. 1- FVoltage-time plots in distinct current densities and duty cycles in 7 minutes.

created coatings in higher currents rises in a constant time and as a result of that the ignition voltage increases. The duty cycle has a major effect on the coating structure by affecting the ignition voltage. As can be seen, increasing the duty cycle from 20 to 80% reduces the ignition voltage. This reduction in ignition voltage is due to the faster growth rate of the coating at higher duty cycles, leading to a coating with lower dielectric resistance. In the lower duty cycle, it seems that the coating procedure is carried out in two steps. Oxidation in the first stage requires more energy in comparison to other specimens to enter the ignition, so at higher voltages, the conditions for ignition are required and after this stage, the ignition is continuously done and at a constant voltage this procedure continues until the end of the coating procedure.

The values of breakdown voltage and the final voltage for the different specimens are indicated in Fig. 2. At high current densities where is the first stage of the process and is a prerequisite for ignition, needs more energy than other specimens to enter the second step. Consequently, the produced oxide in the first stage finds the necessary status for ignition at higher voltages. The final voltage of the specimens rose by rising current density.

When the current density of the oxide film rises, it has higher electrical resistance in the first stage and this makes it need more energy to break the oxide layer. So, it leads to an increase in voltage. Also, as the duty cycle increases, the ignition process occurs at lower voltages. It seems that the longer the duty cycle, the longer the device is on, so most of the procedure is devoted to ignition and growth of coating. Within the duty cycle, ion movement is declined by 20% due to the increase in the shutdown time of the device, and a higher voltage is needed to break the oxide film and produce a spark in the coating procedure.

3.2. Morphology and thickness

SEM images of the coated samples are presented in Fig. 3(a). As can be seen, all coatings have a porous surface due to the formation of sparks

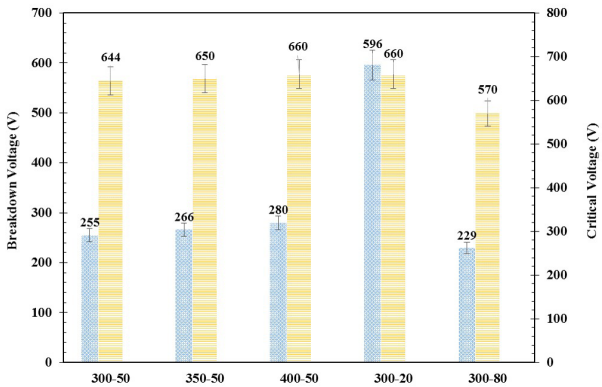

Fig. 2- Values of breakdown and critical voltage for different PEO coated specimens.

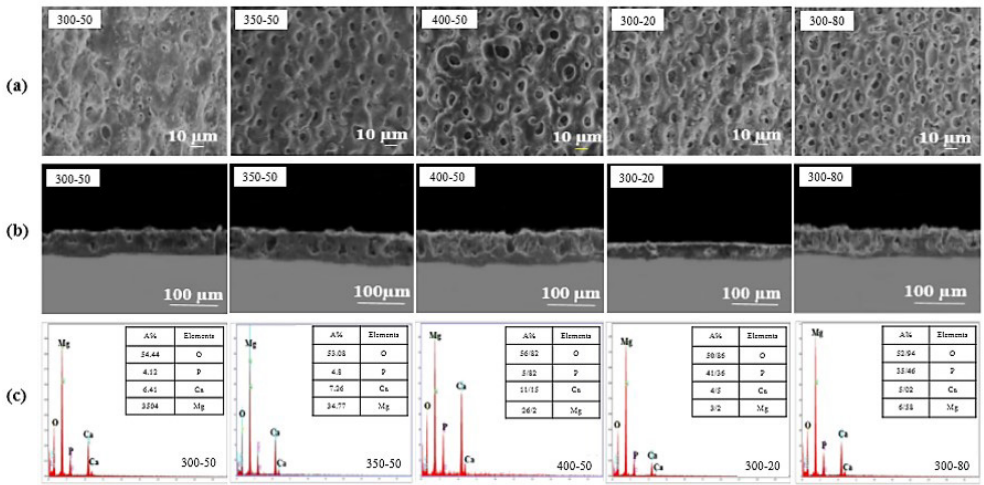

Fig. 3- SEM images of (a) the surface and (b) cross-section for different PEO coated specimens.

during the coating process. The percentage of porosity is indicated in Fig. 4. Cavities are formed when oxide melts and gas bubbles are thrown out of the discharge channels. Solidification of oxide melted by cold electrolyte causes thermal stress in the oxide layer. When these thermal stresses are released, microcracks are formed on the surface. The size of the pores indicates the strength of the discharge. Comparing SEM images of coatings shows that the size of cavities in the coating increases by rising current density. The enlargement of the cavities as a result of rising current density is due to the increase in voltage during the coating process because the amount of energy and heat in the coating has increased. Larger cavities are formed at higher current densities and the effectiveness of cavitation sealing is reduced. In general, at higher current densities, the discharge channels have a higher temperature, so a larger difference in temperature between the coating and the electrolyte causes thermal stresses that result in cracks on the surface. Also, in the high duty cycle and due to the longer time of the circuit, the amount of energy entering the surface increases and it can be expected that the size of the sparks and consequently the cavities in the coating surface will increase. The sample of 300-50 microstructure has almost uniformity and the cavities are almost filled due to sparks with more balanced intensity. The microstructure with less cavities is created during the coating process.

SEM images of the cross-section and thickness of the coatings are shown in Fig. 3(b) and Table 1, respectively. Cross-section pictures clearly reveal that the thickness of the coating has increased by rising current density. There are also many holes in the higher amounts of current density that correspond to the observations of surface images [37]. Based on the obtained results from the voltage-time diagram, at higher current densities, the ignition voltage increases resulting in high energy and heat input during the coating process. This creates larger discharge channels and lets particles penetrate more easily. Under these conditions, the oxide layer formation rate increases, and more molten material is deposited on the surface. According to the presented images and the values of the coatings thickness, it is determined that the thickness of the coating increases by rising the duty cycle. In the higher duty cycle and due to the rise in the time of on mode of device and as a result of rising the coating time, more opportunity is provided for the growth of the coating and as a result, the thickness of the coating increases. In the lower duty cycle, although the ignition voltage is high, the circuit setting time during the coating process is short that results in a reduction in the thickness of the coating.

Fig. 5 shows the distribution map of the major elements within the cross-sectional area and surface of the specimen of 50-300. The elements of the coating contain magnesium, oxygen, phosphorus, and calcium. Magnesium is the main element in the substrate. Based on the obtained results during the procedure of producing the coating, the substrate melts and enters the compounds of the coating. Sparks cause the adsorption in addition to the trapping of nanoparticles. In addition, calcium and phosphorus are present in the form of

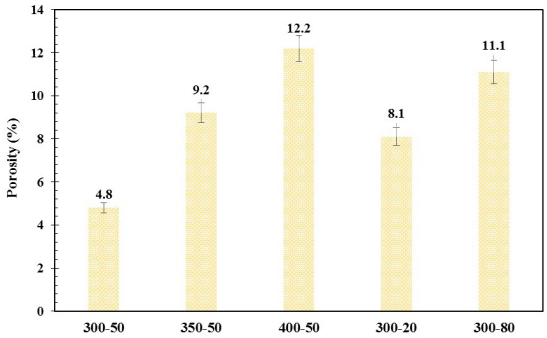

Fig. 4- The average size of surface porosity of coatings obtained from different specimens.

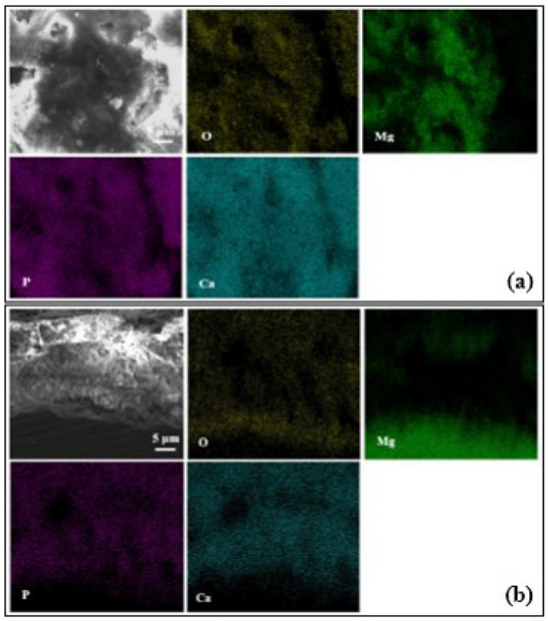

Fig. 5- Distribution map of the main constituent elements from the surface and cross-section of the coating.

hydroxyapatite that shows the uniform distribution of calcium and phosphorus in the existence of hydroxyapatite in the coating. The distribution map of the major elements in the cross-sectional area of the coating indicates that by moving away from the substrate and attaining the outer film, the amount of Mg is obviously less. While the existence of oxygen from the substrate to the surface of the coating has augmented that indicates the production of an oxide layer on the surface. The distribution of calcium and phosphorus shows that they are uniformly distributed throughout the cross-section.

3.3. Composition of Coating

XRD pattern analysis was carried out on Mg alloy of AZ31B. In addition, the XRD pattern obtained by the Grazing method of 50-300 coating is shown in Fig. 6 (a, b).

The spectrum of the XRD pattern using the Grazing method after coating operation shows the production of phases in the coating. The hydroxyapatite nanoparticles are small enough to be entered the coating through the discharge channels and settle into the coating cavities. The peak of hydroxyapatite indicates the neutral entry of nanoparticles into the coating. These nanoparticles entered the coating without changing their chemical composition. The existence of $Mg_3(PO_4)_2$ phase indicates the reaction between the anions obtained from the phosphate salt and the cation obtained from the dissolution of the substrate. The existence of the Mg oxide phase is as a result of the melting of the substrate and its oxidation. The results of EDS obtained from the surface of the produced specimens and the values of its elements in various current densities and different duty cycles are illustrated in Table 2.

The main elements of PEO-derived coatings include calcium, phosphorus, magnesium, and oxygen. As the current density increases, the elements of calcium, phosphorus, and oxygen take part in the growth stages of the coating and their amounts rise. Also, the coated specimen in the duty cycle is 80% more absorbed due to the increase in time of coating and the participation of particles in the coating and due to more sparks, it has absorbed more calcium and phosphorus in comparison to the other two specimens. Nevertheless, as the current density increases, the atomic percentage of magnesium decreases due to the thicker coating. Hydroxyapatite nanoparticles in the coating electrolyte have zeta-negative potential. These particles migrate to the magnesium specimen (positive pole) under the effect of a strong electric field between the anode and the cathode. High adsorption of hydroxyapatite nanoparticles occurs due to high discharge energy. The particles are put inside the pores via electrophoretic force. As the current density increases, this force increases and causes more nanoparticles to enter the coating.

Table 2- EDS analysis from the different coating

Elements (A %)	300-50	350-50	400-50	300-20	300-80
O	54.44	53.08	56.82	50.86	52.94
P	4.12	4.8	5.82	41.36	35.46
Ca	6.41	7.26	11.15	4.5	5.02
Mg	35.4	34.77	26.2	3.2	6.58

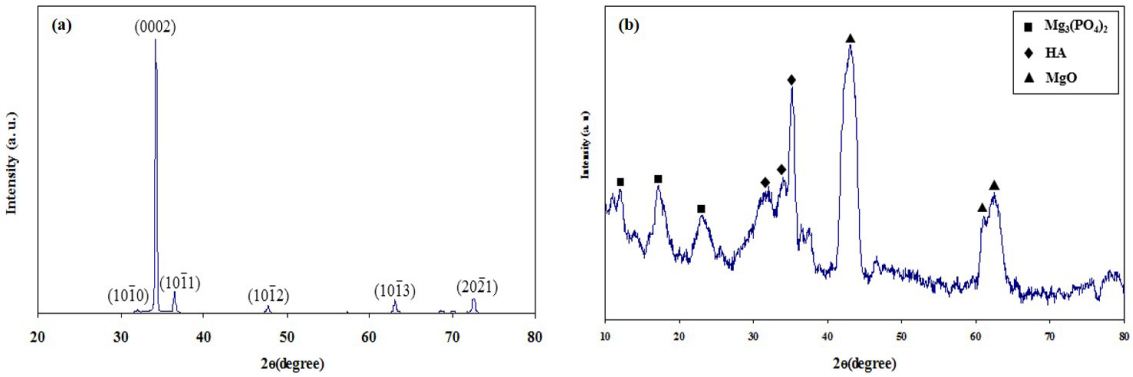

Fig. 6- (a) XRD pattern of the substrate and (b) GXRD pattern by grazing method at 300-50.

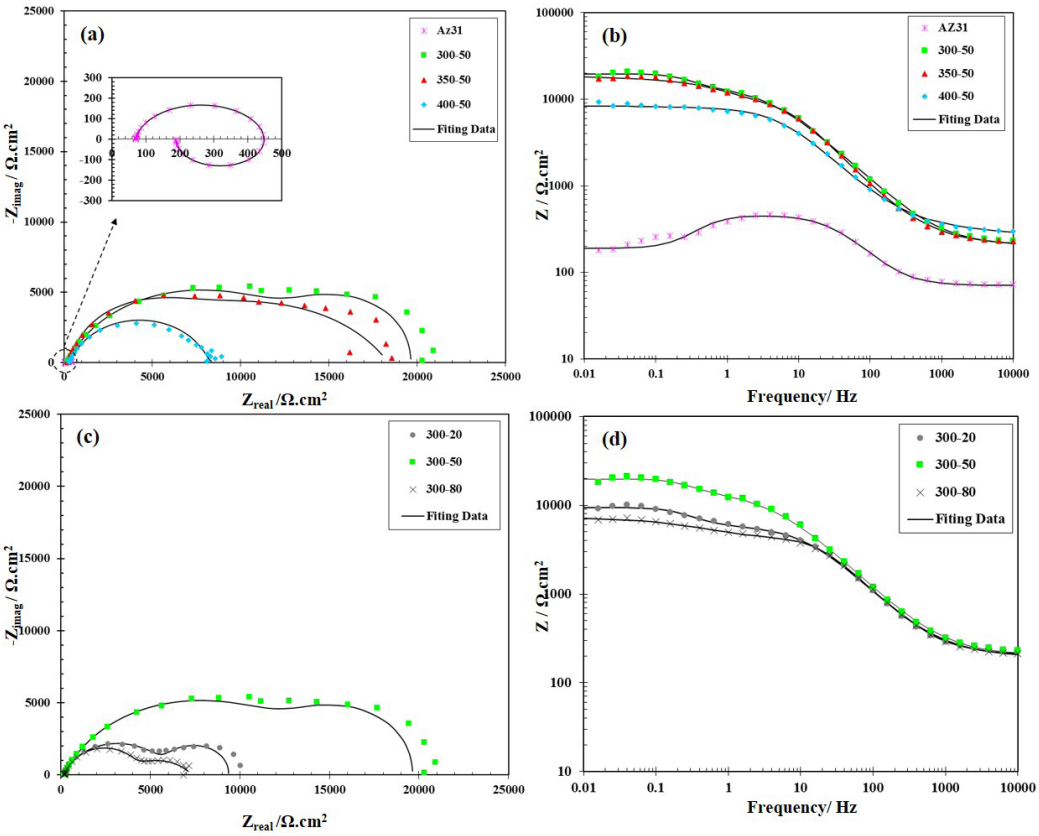

Fig. 7- Nyquist and Bode curves of PEO coated samples in (a, b) different current densities, and (c, d) different duty cycles.

3.4. Corrosion properties

Fig. 7 reveals the EIS plots for all specimens at different current densities and duty cycles. In the Nyquist curves, the real part is plotted on the imaginary part after 1800 s of immersion in the SBF solution. The Nyquist plots reveal that the AZ31B has an inductive behavior as a porous oxide film is formed on the magnesium alloys while exposing the atmosphere and when exposed to a corrosive solution. Due to the low corrosion resistance of this oxide film, the corrosive electrolyte passes through it and reaches the AZ31B substrate, causing inductive behavior [78–80]. All coatings contain two capacitive loops that reveal the existence of two processes. The created loop in high-frequencies corresponds to the outer porous film and at medium frequencies reveals a dense inner film [81,82]. Bode plots show there is a linear region in the plot that the value of impedance in this part indicates the resistance of the solution at high-frequencies. The proposed equivalent circuit is indicated in Fig. 8 to investigate the corrosion behavior of the coated sample. A detailed description of this equivalent circuit can be found in previous publication [23].

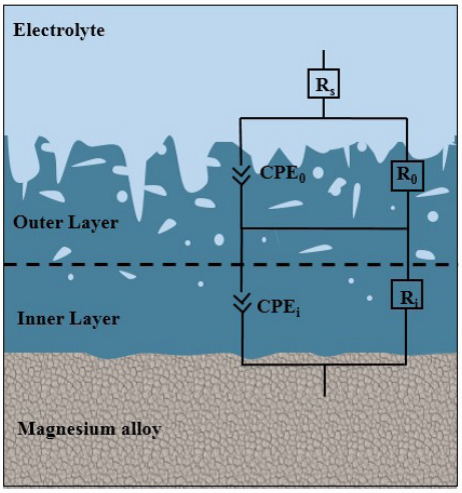

Fig. 8- The equivalent circuit for modeling the corrosion behavior of PEO coated samples.

In this regard, Raffle et al. [83] investigated the coating current density (120, 60, 30 mA / cm²) on the corrosion behavior in NaCl solution. The results showed that with increasing current density due to more intense plasma discharge, the coatings created are very porous. Also, the results

of the corrosion test showed that the best corrosion behavior of low coating current density is due to the dense structure.

In the case that the Nyquist plot does not have a complete semicircle, a constant phase element (CPE) is used instead of a capacitor in the proposed equivalent circuit. The following equation illustrates that the impedance of CPE:

$$Z_{CPE} = \frac{1}{Y_0\ (jW)^n} \quad (1)$$

In this equation, Z_{CPE} is the impedance of the CPE, W is the angular frequency, j is the square root of the imaginary number, and n and Y_0 are frequency-independent parameters. Generally, the value of n can be between 0 and 1 that is a measure of surface heterogeneity [84–86]. The obtained values from modeling the corrosion behavior of coatings are listed in Table 3. According to Table 3, the resistance of the inner film of the coated samples is higher than the resistance of the outer film indicating that the inner layer has a more important role in corrosion protection due to defects and less cavities. The results show that the created coating at higher current density, despite the increase in coating thickness arising from the increase in the intensity of sparks have more cavities and defects on the surface of the coating. These sparks destroy the surface layer and the inner layer leading to the reduction of corrosion resistance. Also, the coating formed in the high duty cycle has greatly reduced its corrosion performance due to the formation of larger cavities and porous structure, because destructive ions can easily pass through the pores and diminish the corrosion resistance. The results showed that the produced coating at a current density of 300 mA/dcm^2 and a duty cycle of 50% has the least resistance of the inner film (13.82 MΩ.cm^2) and the resistance of the outer film (5.63 MΩ.cm^2) and therefore has the best corrosion behavior.

Table 3- Extracted results from the proposed equivalent circuit

Code	R_{inner} (MΩ.cm^2)	R_{outer} (MΩ.cm^2)
300-50	13.82	5.63
350-50	13.31	4.84
400-50	7.63	1.02
300-20	7.3	3.13
300-80	4.64	3.1

PDP plots of the uncoated specimen and the coated specimens in the corrosive SBF solution for 30 minutes are presented in Fig. 9 (a, b). Applying ceramic coatings on AZ31B alloy, PDP plots of all specimens are transferred to a lower corrosion current density (i_{corr}) and more negative potential in comparison to the substrate.

Table 4 shows the extracted results from these graphs. The polarization resistance (R_{pol}) can be

Table 4- Extracted electrochemical results from the PDP plots in different specimens

Code	β_a (mV/dec)	β_c (mV/dec)	E_{corr} ($V_{Ag/AgCl}$)	i_{corr} (A.cm^{-2})	R_p (kΩ.cm^2)	P (%)
300-50	125.51	193.63	-1.551	1×10^{-6}	33.85	13.46
350-50	83.27	106.29	-1.560	7.06×10^{-6}	28.7	15.88
400-50	82.72	74.71	-1.481	8.85×10^{-6}	19.24	23.05
300-20	125.51	193.63	-1.543	8.21×10^{-6}	21.41	21.24
300-80	82.72	74.71	-1.551	9.16×10^{-6}	14.27	31.48

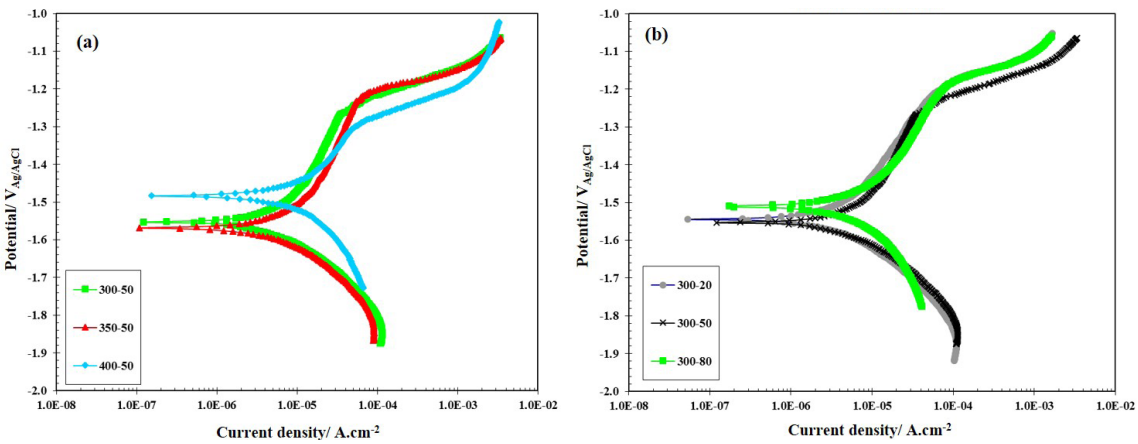

Fig. 9- PDP plots of PEO coated samples in (a) different current densities and (b) different duty cycles.

measured using Eq. (2) [87]:

$$R_{pol} = \frac{\beta_a \beta_c}{2.3(\beta_a + \beta_c) i_{corr}} \quad (2)$$

In this equation, β_a and β_c are called the slope of the anodic and cathodic branches, respectively [88]. The percentage of porosity (*P*) is calculated using the following equation:

$$P = \left(\frac{Rps}{Rp}\right) \times 10^{-\left(\frac{\Delta Ecorr}{\beta a}\right)} \times 100 \quad (3)$$

In this equation, R_{ps} and R_p show the corrosion resistance of the substrate and the coating, β_a is the slope of the substrate anodic branch and ΔE_{corr} depicts the corrosion potential difference between the substrate and the coating, respectively. According to the obtained results, it was realized that the specimens with coating have more polarization resistance in comparison to the substrate of magnesium. Porosity is the most important defect in the coatings because the corrosive electrolyte can easily penetrate into the coating through these porosities and at last get to the substrate by destroying the coating [89,90]. As a result, porosity plays an important role in various properties of the coating, in particular in its corrosion resistance. The results show that corrosion resistance increases by about 50% at the lowest current density and also in the duty cycle. The reason for this is to create a denser coating with a lower porosity percentage.

3.5. bioactivity

In vitro tests are performed outside the living system of organism and keep environmental conditions such as pH and temperature at a certain level. The ability to form bone grafts on biomaterials is often assessed by *in vitro* tests by using body simulated fluid that has a similar electrolyte composition close to human blood plasma. converting inactive surface to bioactive surface and increasing corrosion resistance are useful [91–95]. In general, one of the conditions for implantation to connect with living bone is the formation of a layer of hydroxyapatite on the surface that plays an important role in the formation of secondary apatite, or in other words, the ability to make an increase and encourage the formation of new bone tissue around itself [96–100].

After being immersed in SBF, phosphorus atoms on the surface of HAP-based help to an increase in ionic activity between the surrounding fluid and surface and form phosphate ions on the surface and then, there are positively charged calcium ions in SBF with electrostatic interactions through immersion in body temperature. After rising the concentration of calcium ions on the PEO surface, the PEO surface became positively charged. To balance the positively charged level, the negatively charged phosphate ions migrated to the positively charged PEO level and then, the phosphate and calcium ions reacted with immersion together, resulting in the deposition of secondary apatite at the level of PEO. Then, apatite structures grew spontaneously as more ions entered and coated the entire surface [101].

The study of bioactive behavior was performed for 50-300 samples. Fig. 10 shows SEM images of coated specimens at magnifications of 500 and 1000 after immersion in body simulated fluid. To evaluate the bioactivity, the coated samples in

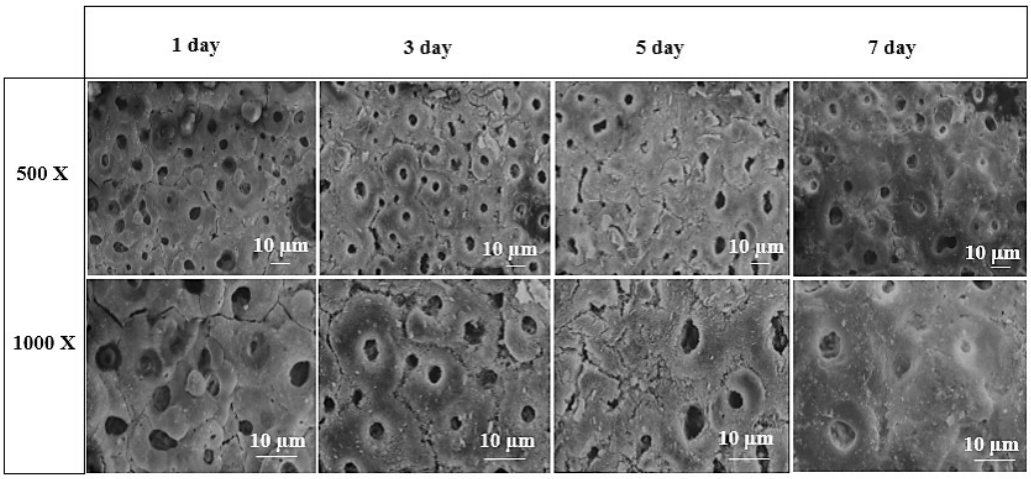

Fig. 10- SEM images of the surface of coatings created at different immersion times.

SBF solution were immersed for different periods of 1, 3, 5, and 7 and their surface was examined for their microstructure. The results show that by putting the samples in the simulated body fluid, particles of apatite are formed in the form of white and spherical areas in the shape on the surface of the hydroxyapatite samples that results in a rapid reaction. Better and better the biomaterial is in contact with the natural tissues of the body. The presence of cavities in the microscopic images indicate the dissolution of hydroxyapatite in a part of the surface and prominent areas indicate the formation of apatite deposits on the surface that shows bone-like apatite. According to the sample image which was immersed in body simulated fluid for 1 day, it was observed that no significant change in morphology was observed and apparently no apatite was formed on the coating or the rate of apatite formation in the early times. It is very insignificant as the immersion time increases, as shown in the figure, the sample that has been immersed in the body simulated fluid for 7 days, is clearly exposed to apatite. As the immersion time in the simulator solution increases, more hydroxyapatite spheres are formed on the surface of the specimen and the cavities on the surface of the coating are filled with deposited particles.

The long-term corrosion response and growth ability of hydroxyapatite in coatings that were obtained in SBF solution are investigated using the immersion test. According to Fig. 11, the EIS plots of the coated specimens are observed at different immersion times of 1, 3, 5, and 7 days.

As can be observed, the resistance of the inner and outer layers increases by increasing the time of immersion. The presence of a hydroxyapatite layer in the coatings can cause the deposition of calcium phosphate which in turn increases the resistance of the outer layer because the products of corrosion and deposition are more within these defects. The cavities in the coatings are gradually sealed by the deposition and accumulation of corrosion products. In addition, this can help to an increase in the coating impedance to some extent.

To model the electrochemical behavior of the coatings at different times of immersion, the equivalent circuit of Fig. 8 was used. The results obtained from the proposed equivalent circuit are shown in Table 5. According to Table 5, the resistance of the inner and outer layers will increase by increasing the time of immersion. By rising the immersion time up to 7 days, the resistance of the inner and film has rose by 55% and so the resistance of the outer film rose by 86%.

4. Conclusion

In this study, the corrosion behavior of coatings formed by the PEO process on Mg alloy of AZ31B was studied and the following conclusions were obtained:

1. Coatings created by the PEO method indicate that the surface of the coatings is porous. The results show that by changing and controlling the operating parameters, the amount of porosity can be reduced and thus the corrosion behavior of coatings can be improved. Also, the phase analysis of the coating shows that the $Mg_3(PO_4)_2$ phase

Table 5- Extracted results from the proposed equivalent circuit

Code	R_{inner} (MΩ.cm^2)	R_{outer} (MΩ.cm^2)
30 min	13.82	5.63
1 day	14.51	19.72
3 day	29.03	29.14
5 day	30.2	37.2
7 day	31.4	42.12

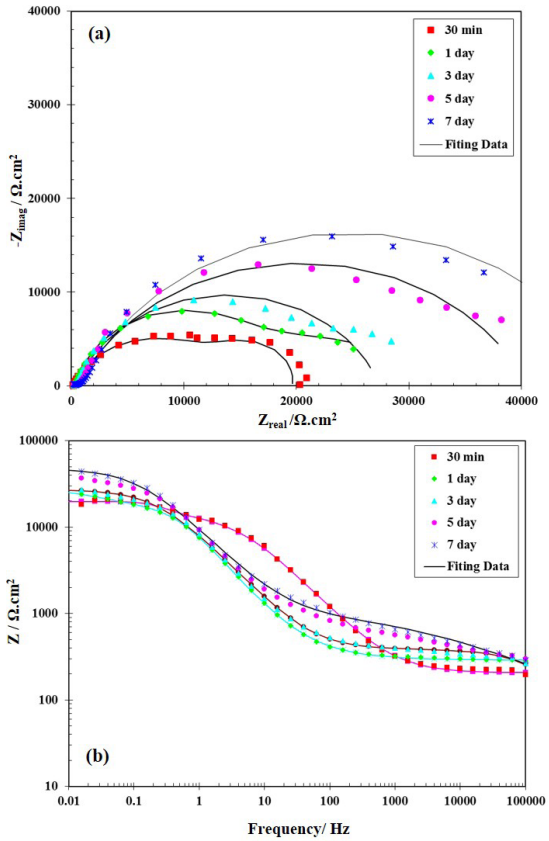

Fig. 11- (a)Nyquist and (b) Bode curves of PEO coated samples at different times of immersion.

indicates the reaction between the anions from the phosphate salt and the cation from the dissolution of the substrate. The presence of magnesium oxide phase is due to the melting of the substrate and its oxidation.

2.The results indicated that by an increase in the current density resulted in an increase in the percentage of porosity from 4.8 to 12.2% and the thickness of the coatings from 36.1 to 45.3 micrometers. The results of electrochemical measurements showed that the coating produced in the current density of 300 mA/dm^2 has the least corrosion current density (1×10^{-6} A/cm^2) and the most polarization resistance was (33.85 $M\Omega.cm^2$) among the specimens.

3. Investigations carried out on the effect of the duty cycle (20, 50, and 80%) showed that the produced coating in 50% duty cycle has the least porosity (4.8%) on the surface and the least corrosion current density (1×10^{-6} A/cm^2) and the highest polarization resistance (33.85 $M\Omega.cm^2$) was among the specimens.

4. Studies on the effect of immersion time (1, 3, 5, and 7 days) showed that by rising immersion time, the amount of apatite produced on the surface increased. In addition, the results of EIS in the body simulated fluid showed that the corrosion resistance of the outer film augmented by 86% and the inner film by 55% after 7 days of immersion. The formation of bio-apatite deposits on the surface of the coating after 7 days of immersion in the simulated solution depicts the bioactivity of the coating.

References

1. Ali M, Elsherif M, Salih AE, Ul-Hamid A, Hussein MA, Park S, et al. Surface modification and cytotoxicity of Mg-based bio-alloys: An overview of recent advances. Journal of Alloys and Compounds. 2020;825:154140.
2. Riaz U, Shabib I, Haider W. The current trends of Mg alloys in biomedical applications—A review. Journal of Biomedical Materials Research Part B: Applied Biomaterials. 2019;107(6):1970-96.
3. Chaharmahali R, Fattah-alhosseini A, Babaei K. Surface characterization and corrosion behavior of calcium phosphate (Ca-P) base composite layer on Mg and its alloys using plasma electrolytic oxidation (PEO): A review. Journal of Magnesium and Alloys. 2020;9(1):21-40.
4. Gray JE, Luan B. Protective coatings on magnesium and its alloys — a critical review. Journal of Alloys and Compounds. 2002;336(1-2):88-113.
5. Zhang Y, Yan C. Development of anodic film on Mg alloy AZ91D. Surface and Coatings Technology. 2006;201(6):2381-6.
6. Bedghiou D, Reguig FH, Boumaza A. Novel high/ultrahigh pressure structures of TiO2 with low band gaps. Computational Materials Science. 2019;166:303-10.
7. Hornberger H, Virtanen S, Boccaccini AR. Biomedical coatings on magnesium alloys – A review. Acta Biomaterialia. 2012;8(7):2442-55.
8. Sezer N, Evis Z, Kayhan SM, Tahmasebifar A, Koç M. Review of magnesium-based biomaterials and their applications. Journal of Magnesium and Alloys. 2018;6(1):23-43.
9. Toorani M, Aliofkhazraei M. Review of electrochemical properties of hybrid coating systems on Mg with plasma electrolytic oxidation process as pretreatment. Surfaces and Interfaces. 2019;14:262-95.
10. Mueller W-D, Lucia Nascimento M, Lorenzo de Mele MF. Critical discussion of the results from different corrosion studies of Mg and Mg alloys for biomaterial applications . Acta Biomaterialia. 2010;6(5):1749-55.
11. Chandra G, Pandey A. Preparation Strategies for Mg-alloys for Biodegradable Orthopaedic Implants and Other Biomedical Applications: A Review. IRBM. 2020.
12. Jacobs A, Renaudin G, Forestier C, Nedelec J-M, Descamps S. Biological properties of copper-doped biomaterials for orthopedic applications: A review of antibacterial, angiogenic and osteogenic aspects. Acta Biomaterialia. 2020;117:21-39.
13. Zhou H, Liang B, Jiang H, Deng Z, Yu K. Magnesium-based biomaterials as emerging agents for bone repair and regeneration: From mechanism to application. Journal of Magnesium and Alloys. 2021 Apr 6.
14. Fattah-alhosseini A, Chaharmahali R, Babaei K. Effect of particles addition to solution of plasma electrolytic oxidation (PEO) on the properties of PEO coatings formed on magnesium and its alloys: A review. Journal of Magnesium and Alloys. 2020;8(3):799-818.
15. Liu D, Yang D, Li X, Hu S. Mechanical properties, corrosion resistance and biocompatibilities of degradable Mg-RE alloys: A review. Journal of Materials Research and Technology. 2019;8(1):1538-49.
16. Dehghan-Manshadi A, Yu P, Dargusch M, StJohn D, Qian M. Metal injection moulding of surgical tools, biomaterials and medical devices: A review. Powder Technology. 2020;364:189-204.
17. Harada Y, Kumai S. Effect of ceramics coating using sol–gel processing on corrosion resistance and age hardening of AZ80 magnesium alloy substrate. Surface and Coatings Technology. 2013;228:59-67.
18. Kuo Y-L, Chang K-H. Atmospheric pressure plasma enhanced chemical vapor deposition of SiOx films for improved corrosion resistant properties of AZ31 magnesium alloys. Surface and Coatings Technology. 2015;283:194-200.
19. Yadav VS, Sankar MR, Pandey LM. Coating of bioactive glass on magnesium alloys to improve its degradation behavior: Interfacial aspects. Journal of Magnesium and Alloys. 2020;8(4):999-1015.
20. Rahman M, Li Y, Wen C. HA coating on Mg alloys for biomedical applications: A review. Journal of Magnesium and Alloys. 2020;8(3):929-43.
21. Keyvani A, Zamani M, Fattah-Alhosseini A, Nourbakhsh SH, Bahamirian M. Microstructure and corrosion resistance of MAO coatings on AZ31 magnesium. Materials Research Express. 2018;5(8):086510.
22. Yadav VS, Sankar MR, Pandey LM. Coating of bioactive glass on magnesium alloys to improve its degradation behavior: Interfacial aspects. Journal of Magnesium and Alloys. 2020 Dec 1;8(4):999-1015.
23. Catauro M, Papale F, Sapio L, Naviglio S. Biological influence of Ca/P ratio on calcium phosphate coatings by sol-gel processing. Materials Science and Engineering: C. 2016;65:188-93.

24. Vakili-Azghandi M, Fattah-alhosseini A, Keshavarz MK. Effects of Al2O3 Nano-Particles on Corrosion Performance of Plasma Electrolytic Oxidation Coatings Formed on 6061 Aluminum Alloy. Journal of Materials Engineering and Performance. 2016;25(12):5302-13.
25. Lin M, Nemcova A, Voevodin AA, Korenyi-Both A, Liskiewicz TW, Laugel N, et al. Surface characteristics underpinning fretting wear performance of heavily loaded duplex chameleon/PEO coatings on Al. Tribology International. 2021;154:106723.
26. Fattah-Alhosseini A, Vakili-Azghandi M, Keshavarz MK. Influence of Concentrations of KOH and Na2SiO3 Electrolytes on the Electrochemical Behavior of Ceramic Coatings on 6061 Al Alloy Processed by Plasma Electrolytic Oxidation. Acta Metallurgica Sinica (English Letters). 2016;29(3):274-81.
27. Vakili-Azghandi M, Fattah-alhosseini A, Keshavarz MK. Optimizing the electrolyte chemistry parameters of PEO coating on 6061 Al alloy by corrosion rate measurement: Response surface methodology. Measurement. 2018;124:252-9.
28. Wu Y-k, Yang Z, Wang R-q, Wu G-r, Chen D, Wang D-d, et al. An investigation of microstructure evolution for plasma electrolytic oxidation (PEO) coated Al in an alkaline silicate electrolyte. Surface and Coatings Technology. 2018;351:136-52.
29. Fattah-alhosseini A, Gashti SO, Molaie M. Effects of Disodium Phosphate Concentration (Na2HPO4·2H2O) on Microstructure and Corrosion Resistance of Plasma Electrolytic Oxidation (PEO) Coatings on 2024 Al Alloy. Journal of Materials Engineering and Performance. 2018;27(2):825-34.
30. Shi X, Wang Y, Li H, Zhang S, Zhao R, Li G, et al. Corrosion resistance and biocompatibility of calcium-containing coatings developed in near-neutral solutions containing phytic acid and phosphoric acid on AZ31B alloy. Journal of Alloys and Compounds. 2020;823:153721.
31. Keyvani A, Zamani M, Bahamirian M, Nikoomanzari E, Fattah-alhosseini A, Sina H. Role of incorporation of ZnO nanoparticles on corrosion behavior of ceramic coatings developed on AZ31 magnesium alloy by plasma electrolytic oxidation technique. Surfaces and Interfaces. 2020;22:100728.
32. Monetta T, Parnian P, Acquesta A. Recent Advances in the Control of the Degradation Rate of PEO Treated Magnesium and Its Alloys for Biomedical Applications. Metals. 2020;10(7):907.
33. Zhang Y, Chen F, Zhang Y, Liu Z, Wang X, Du C. Influence of graphene oxide on the antiwear and antifriction performance of MAO coating fabricated on Mg Li alloy. Surface and Coatings Technology. 2019;364:144-56.
34. Mashtalyar DV, Sinebryukhov SL, Imshinetskiy IM, Gnedenkov AS, Nadaraia KV, Ustinov AY, et al. Hard wearproof PEO-coatings formed on Mg alloy using TiN nanoparticles. Applied Surface Science. 2020;503:144062.
35. Tang H, Wang F. Synthesis and properties of CaTiO3-containing coating on AZ31 magnesium alloy by micro-arc oxidation. Materials Letters. 2013;93:427-30.
36. Sreekanth D, Rameshbabu N. Development and characterization of MgO/hydroxyapatite composite coating on AZ31 magnesium alloy by plasma electrolytic oxidation coupled with electrophoretic deposition. Materials Letters. 2012;68:439-42.
37. Yang J, Lu X, Blawert C, Di S, Zheludkevich ML. Microstructure and corrosion behavior of Ca/P coatings prepared on magnesium by plasma electrolytic oxidation. Surface and Coatings Technology. 2017;319:359-69.
38. Dou J, Wang C, Gu G, Chen C. Formation of silicon-calcium-phosphate-containing coating on Mg-Zn-Ca alloy by a two-step micro-arc oxidation technique. Materials Letters. 2018;212:37-40.
39. Attarzadeh N, Ramana CV. Plasma Electrolytic Oxidation Ceramic Coatings on Zirconium (Zr) and ZrAlloys: Part I—Growth Mechanisms, Microstructure, and Chemical Composition. Coatings. 2021;11(6):634.
40. Attarzadeh N, Ramana CV. Plasma Electrolytic Oxidation Ceramic Coatings on Zirconium (Zr) and Zr-Alloys: Part-II: Properties and Applications. Coatings. 2021;11(6):620.
41. Aktug SL, Kutbay I, Usta M. Characterization and formation of bioactive hydroxyapatite coating on commercially pure zirconium by micro arc oxidation. Journal of Alloys and Compounds. 2017;695:998-1004.
42. Aktuğ SL, Durdu S, Yalçın E, Çavuşoğlu K, Usta M. In vitro properties of bioceramic coatings produced on zirconium by plasma electrolytic oxidation. Surface and Coatings Technology. 2017;324:129-39.
43. Sandhyarani M, Rameshbabu N, Venkateswarlu K, Sreekanth D, Subrahmanyam C. Surface morphology, corrosion resistance and in vitro bioactivity of P containing ZrO2 films formed on Zr by plasma electrolytic oxidation. Journal of Alloys and Compounds. 2013;553:324-32.
44. Nikoomanzari E, Fattah-alhosseini A, Pajohi Alamoti MR, Keshavarz MK. Effect of ZrO2 nanoparticles addition to PEO coatings on Ti–6Al–4V substrate: Microstructural analysis, corrosion behavior and antibacterial effect of coatings in Hank's physiological solution. Ceramics International. 2020;46(9):13114-24.
45. Roknian M, Fattah-alhosseini A, Gashti SO, Keshavarz MK. Study of the effect of ZnO nanoparticles addition to PEO coatings on pure titanium substrate: Microstructural analysis, antibacterial effect and corrosion behavior of coatings in Ringer's physiological solution. Journal of Alloys and Compounds. 2018;740:330-45.
46. Hwang I-J, Choe H-C. Surface morphology and cell behavior of Zn-coated Ti-6Al-4V alloy by RF-sputtering after PEO-treatment. Surface and Coatings Technology. 2019;361:386-95.
47. Lim S-G, Choe H-C. Bioactive apatite formation on PEO-treated Ti-6Al-4V alloy after 3rd anodic titanium oxidation. Applied Surface Science. 2019;484:365-73.
48. Park M-G, Choe H-C. Corrosion behaviors of bioactive element coatings on PEO-treated Ti-6Al-4V alloys. Surface and Coatings Technology. 2019;376:44-51.
49. Molaei M, Fattah-Alhosseini A, Gashti SO. Sodium Aluminate Concentration Effects on Microstructure and Corrosion Behavior of the Plasma Electrolytic Oxidation Coatings on Pure Titanium. Metallurgical and Materials Transactions A. 2018;49(1):368-75.
50. Xue W, Deng Z, Chen R, Zhang T. Growth regularity of ceramic coatings formed by microarc oxidation on Al–Cu–Mg alloy. Thin Solid Films. 2000;372(1-2):114-7.
51. Chaharmahali R, Fattah-alhosseini A, Nouri M, Babaei K. Improving surface characteristics of PEO coatings of Mg and its alloys with zirconia nanoparticles: a review. Applied Surface Science Advances. 2021;6:100131.
52. Arrabal R, Mota JM, Criado A, Pardo A, Mohedano M, Matykina E. Assessment of duplex coating combining plasma electrolytic oxidation and polymer layer on AZ31 magnesium alloy. Surface and Coatings Technology. 2012;206(22):4692-703.
53. Critchlow GW, Yendall KA, Bahrani D, Quinn A, Andrews F. Strategies for the replacement of chromic acid anodising for the structural bonding of aluminium alloys. International Journal of Adhesion and Adhesives. 2006;26(6):419-53.
54. Lou BS, Lee JW, Tseng CM, Lin YY, Yen CA. Mechanical property and corrosion resistance evaluation of AZ31 magnesium alloys by plasma electrolytic oxidation treatment: effect of MoS2 particle addition. Surface and Coatings

Technology. 2018 Sep 25;350:813-22.
55. Fattah-alhosseini A, Chaharmahali R, Keshavarz MK, Babaei K. Surface characterization of bioceramic coatings on Zr and its alloys using plasma electrolytic oxidation (PEO): A review. Surfaces and Interfaces. 2021;25:101283.
56. Hu Y, Meng J, Luan X, Dong X, Zhou H, Qu L, et al. Plasma electrolytic oxidation of Ti-6Al-4V alloy and its influence on the machinability during micro-milling. Measurement. 2021;170:108719.
57. Clyne TW, Troughton SC. A review of recent work on discharge characteristics during plasma electrolytic oxidation of various metals. International Materials Reviews. 2019;64(3):127-62.
58. Wang Y, Yu H, Chen C, Zhao Z. Review of the biocompatibility of micro-arc oxidation coated titanium alloys. Materials & Design. 2015;85:640-52.
59. Barati Darband G, Aliofkhazraei M, Hamghalam P, Valizade N. Plasma electrolytic oxidation of magnesium and its alloys: Mechanism, properties and applications. Journal of Magnesium and Alloys. 2017;5(1):74-132.
60. Fattah-alhosseini A, Molaei M, Attarzadeh N, Babaei K, Attarzadeh F. On the enhanced antibacterial activity of plasma electrolytic oxidation (PEO) coatings that incorporate particles: A review. Ceramics International. 2020;46(13):20587-607.
61. Simchen F, Sieber M, Kopp A, Lampke T. Introduction to Plasma Electrolytic Oxidation—An Overview of the Process and Applications. Coatings. 2020;10(7):628.
62. Lu X, Mohedano M, Blawert C, Matykina E, Arrabal R, Kainer KU, et al. Plasma electrolytic oxidation coatings with particle additions – A review. Surface and Coatings Technology. 2016;307:1165-82.
63. Ding Z-Y, Cui L-Y, Chen X-B, Zeng R-C, Guan S-K, Li S-Q, et al. In vitro corrosion of micro-arc oxidation coating on Mg-1Li-1Ca alloy — The influence of intermetallic compound Mg2Ca. Journal of Alloys and Compounds. 2018;764:250-60.
64. Durdu S, Usta M. Characterization and mechanical properties of coatings on magnesium by micro arc oxidation. Applied Surface Science. 2012;261:774-82.
65. Lu X, Blawert C, Mohedano M, Scharnagl N, Zheludkevich ML, Kainer KU. Influence of electrical parameters on particle uptake during plasma electrolytic oxidation processing of AM50 Mg alloy. Surface and Coatings Technology. 2016;289:179-85.
66. Xiang N, Song R-g, Zhuang J-j, Song R-x, Lu X-y, Su X-p. Effects of current density on microstructure and properties of plasma electrolytic oxidation ceramic coatings formed on 6063 aluminum alloy. Transactions of Nonferrous Metals Society of China. 2016;26(3):806-13.
67. Dehnavi V, Luan BL, Shoesmith DW, Liu XY, Rohani S. Effect of duty cycle and applied current frequency on plasma electrolytic oxidation (PEO) coating growth behavior. Surface and Coatings Technology. 2013;226:100-7.
68. Bala Srinivasan P, Liang J, Balajeee RG, Blawert C, Störmer M, Dietzel W. Effect of pulse frequency on the microstructure, phase composition and corrosion performance of a phosphate-based plasma electrolytic oxidation coated AM50 magnesium alloy. Applied Surface Science. 2010;256(12):3928-35.
69. Arunnellaiappan T, Kishore Babu N, Rama Krishna L, Rameshbabu N. Influence of frequency and duty cycle on microstructure of plasma electrolytic oxidized AA7075 and the correlation to its corrosion behavior. Surface and Coatings Technology. 2015;280:136-47.
70. Lin X, Wang X, Tan L, Wan P, Yu X, Li Q, et al. Effect of preparation parameters on the properties of hydroxyapatite containing micro-arc oxidation coating on biodegradable ZK60 magnesium alloy. Ceramics International. 2014;40(7):10043-51.
71. Tang Y, Zhao X, Jiang K, Chen J, Zuo Y. -The influences of duty cycle on the bonding strength of AZ31B magnesium alloy by microarc oxidation treatment. Surface and Coatings Technology. 2010;205(6):1789-92.
72. Kokubo T, Takadama H. How useful is SBF in predicting in vivo bone bioactivity? Biomaterials. 2006;27(15):2907-15.
73. Fattah-alhosseini A, Babaei K, Molaei M. Plasma electrolytic oxidation (PEO) treatment of zinc and its alloys: A review. Surfaces and Interfaces. 2020;18:100441.
74. Chang L, Tian L, Liu W, Duan X. Formation of dicalcium phosphate dihydrate on magnesium alloy by micro-arc oxidation coupled with hydrothermal treatment. Corrosion Science. 2013;72:118-24.
75. Guan Y-j, Xia Y. Correlation between discharging property and coatings microstructure during plasma electrolytic oxidation. Transactions of Nonferrous Metals Society of China. 2006;16(5):1097-102.
76. Lu X, Blawert C, Huang Y, Ovri H, Zheludkevich ML, Kainer KU. Plasma electrolytic oxidation coatings on Mg alloy with addition of SiO2 particles. Electrochimica Acta. 2016 Jan 1;187:20-33.
77. Kaseem M, Fatimah S, Nashrah N, Ko YG. Recent progress in surface modification of metals coated by plasma electrolytic oxidation: Principle, structure, and performance. Progress in Materials Science. 2020;117:100735.
78. King AD, Birbilis N, Scully JR. Accurate Electrochemical Measurement of Magnesium Corrosion Rates; a Combined Impedance, Mass-Loss and Hydrogen Collection Study. Electrochimica Acta. 2014;121:394-406.
79. Kirkland NT, Birbilis N, Staiger MP. Assessing the corrosion of biodegradable magnesium implants: A critical review of current methodologies and their limitations. Acta Biomaterialia. 2012;8(3):925-36.
80. Chaharmahali R, Fattah-Alhosseini A, Esfahani H. Increasing the in-vitro corrosion resistance of AZ31B-Mg alloy via coating with hydroxyapatite using plasma electrolytic oxidation. Journal of Asian Ceramic Societies. 2019;8(1):39-49.
81. Bordbar-Khiabani A, Yarmand B, Mozafari M. Enhanced corrosion resistance and in-vitro biodegradation of plasma electrolytic oxidation coatings prepared on AZ91 Mg alloy using ZnO nanoparticles-incorporated electrolyte. Surface and Coatings Technology. 2019;360:153-71.
82. Zhao J, Xie X, Zhang C. Effect of the graphene oxide additive on the corrosion resistance of the plasma electrolytic oxidation coating of the AZ31 magnesium alloy. Corrosion Science. 2017 Jan 1;114:146-55.
83. Rapheal G, Kumar S, Scharnagl N, Blawert C. Effect of current density on the microstructure and corrosion properties of plasma electrolytic oxidation (PEO) coatings on AM50 Mg alloy produced in an electrolyte containing clay additives. Surface and Coatings Technology. 2016;289:150-64.
84. Atrens A, Shi Z, Mehreen SU, Johnston S, Song G-L, Chen X, et al. Review of Mg alloy corrosion rates. Journal of Magnesium and Alloys. 2020;8(4):989-98.
85. Antunes RA, de Oliveira MCL. Corrosion fatigue of biomedical metallic alloys: Mechanisms and mitigation. Acta Biomaterialia. 2012;8(3):937-62.
86. Singh I. B, Singh M, and Das S. A comparative corrosion behavior of Mg, AZ31 and AZ91 alloys in 3.5% NaCl solution. Journal of Magnesium and Alloys. 2015;3:142-148.
87. Haycock EW. Discussion of "Electrochemical Polarization, 1. A Theoretical Analysis of the Shape of Polarization Curves" [M. Stern and A. L. Geary (pp. 56–63, Vol. 104)]. Journal of The Electrochemical Society. 1957;104(12):751.

88. Shokouhfar M, Allahkaram SR. Effect of incorporation of nanoparticles with different composition on wear and corrosion behavior of ceramic coatings developed on pure titanium by micro arc oxidation. Surface and Coatings Technology. 2017;309:767-78.
89. Lee KM, Shin KR, Namgung S, Yoo B, Shin DH. Electrochemical response of ZrO2-incorporated oxide layer on AZ91 Mg alloy processed by plasma electrolytic oxidation. Surface and Coatings Technology. 2011;205(13-14):3779-84.
90. Gu XN, Li N, Zhou WR, Zheng YF, Zhao X, Cai QZ, et al. Corrosion resistance and surface biocompatibility of a microarc oxidation coating on a Mg–Ca alloy. Acta Biomaterialia. 2011;7(4):1880-9.
91. Wang H, Zhu S, Wang L, Feng Y, Ma X, Guan S. Formation mechanism of Ca-deficient hydroxyapatite coating on Mg–Zn–Ca alloy for orthopaedic implant. Applied Surface Science. 2014;307:92-100.
92. Gopi D, Indira J, Nithiya S, Kavitha L, Mudali UK, Kanimozhi K. Influence of surfactant concentration on nanohydroxyapatite growth. Bulletin of Materials Science. 2013;36(5):799-805.
93. Liu GY, Hu J, Ding ZK, Wang C. Bioactive calcium phosphate coating formed on micro-arc oxidized magnesium by chemical deposition. Applied Surface Science. 2011;257(6):2051-7.
94. Seyfoori A, Mirdamadi S, Seyedraoufi ZS, Khavandi A, Aliofkhazraei M. Synthesis of biphasic calcium phosphate containing nanostructured films by micro arc oxidation on magnesium alloy. Materials Chemistry and Physics. 2013;142(1):87-94.
95. Safavi MS, Walsh FC, Surmeneva MA, Surmenev RA, Khalil-Allafi J. Electrodeposited Hydroxyapatite-Based Biocoatings: Recent Progress and Future Challenges. Coatings. 2021;11(1):110.
96. Yang J, Lu X, Blawert C, Di S, Zheludkevich ML. -Microstructure and corrosion behavior of Ca/P coatings prepared on magnesium by plasma electrolytic oxidation. Surface and Coatings Technology. 2017;319:359-69.
97. Anawati, Asoh H, Ono S. Enhanced uniformity of apatite coating on a PEO film formed on AZ31 Mg alloy by an alkali pretreatment. Surface and Coatings Technology. 2015;272:182-9.
98. Mohammad Salahi Tohidi P, Safavi MS, Etminanfar M, Khalil-Allafi J. Pulsed electrodeposition of compact, corrosion resistant, and bioactive HAp coatings by application of optimized magnetic field. Materials Chemistry and Physics. 2020;254:123511.
99. Safavi MS, Surmeneva MA, Surmenev RA, Khalil-Allafi J. RF-magnetron sputter deposited hydroxyapatite-based composite & multilayer coatings: A systematic review from mechanical, corrosion, and biological points of view. Ceramics International. 2021;47(3):3031-53.
100. No Title, (n.d.). https://doi.org/10.22059/JUFGNSM.2019.01.01.
101. Tang H, Gao Y. Preparation and characterization of hydroxyapatite containing coating on AZ31 magnesium alloy by micro-arc oxidation. Journal of Alloys and Compounds. 2016;688:699-708.